Cracking behavior of tungsten armor under ELM-like thermal shock loads: A computational study

Muyuan Li[a], Ewald Werner[a], Jeong-Ha You[b,*]

[a] *Lehrstuhl für Werkstoffkunde und Werkstoffmechanik, Technische Universität München, Boltzmannstr.15, 85748 Garching, Germany*
[b] *Max-Planck-Institut für Plasmaphysik, Boltzmannstr.2, 85748 Garching, Germany*

Abstract

In this work, the cracking behavior of tungsten under edge-localized mode (ELM)-like thermal shock loads was investigated on the basis of a rigorous computational fracture mechanical analysis combined with the finite element method. Typical transient thermal shock loads of ELM conditions were considered with a relevant range of power density and base temperature for a loading duration of 1 ms. Crack initiation and progressive growth were predicted using the extended finite element method and the J-integral was calculated for the assumed precrack by means of the virtual crack extension method. For a power density of 1 GW/m^2 and higher, a crack is preferably initiated near the edge of the loading area and is then followed by a gradual horizontal kinking, parallel to the loading surface. The crack formation is predicted for the power density of 0.6 GW/m^2 and above, and when the base temperature is higher than 600 °C, almost no cracks is predicted. The numerically predicted cracking behavior agrees in general with the experimental observations.

Keywords: extended finite element method, thermal shock experiments, J-integral, cracking threshold, tungsten cracking

1. Introduction

Tungsten has been considered the most promising armor material for plasma-facing components (PFCs) in fusion devices such as divertor target and first wall. The unique advantage of tungsten as plasma-facing material is due to its exclusively outstanding properties, for example, extremely low sputtering erosion rate, highest melting point, negligibly small solubility of hydrogen, relatively high thermal conductivity, superior strength at elevated temperatures and moderate thermal expansion. In addition to neutron wall load, tungsten-armored PFCs shall be subjected to significant surface heat flux loads due to radiation and particle bombardment from the plasma. In large-scale fusion reactors, such as ITER or DEMO, the stationary heat flux load is expected to reach 10 MW/m^2 during normal plasma operation and up to 20 MW/m^2 during slow transients. The deposited heat shall be exhausted by active cooling in order to keep the surface temperature constant maintaining a steady state operation [1].

On the other hand, the PFCs are supposed to withstand transient thermal loads during transient events where a large amount of energy is deposited onto local areas of the armor surface in a very short period. Such transient thermal loads are induced by three different types of plasma instability taking place during tokamak operation: plasma disruption, vertical displacement event (VDE) and ELMs [2]. These events exhibit different pulse time range and energy release scale, respectively. PFCs are stressed by such thermal transients in form of a repeated thermal shock.

*Corresponding author. Tel.: +49 089 3299 1373; fax:+49 089 3299 1212.
Email address: you@ipp.mpg.de (Jeong-Ha You)

There are plenty of experimental reports on the detrimental impact of thermal transients on the microstructural integrity of tungsten-based materials [3–7]. Typically, a high power electron beam or a plasma beam is used to simulate transient thermal loading with short pulses. One of the most prominent works on this topic is the electron beam irradiation test study conducted by Linke and coworkers [6]. By means of repeated electron beam flashing with ELM-like load conditions (~1 MJ/m^2, ~1 ms), they observed a systematic trend of damage formation and evolution in the irradiated surface layer as a function of the input energy, base temperature, number of pulses and material grade. Typical damage features were cracking and surface roughening due to plastic strains. At lower base temperatures, in particular below the ductile-to-brittle transition temperature, tungsten materials exhibited critical crack formation behavior. This finding suggests that the thermal shock loads by ELMs can considerably reduce the lifetime of tungsten armor posing a crucial design concern for the PFCs of ITER and DEMO. The results of the thermal shock experiments simulating ELM loads manifest a close correlation between the loading parameters (power density, base temperature, etc.) and the resulting cracking patterns. For understanding this relationship on a quantitative basis one needs a rigorous computational assessment of cracking features in the most critical regions.

In this study, the driving force of cracking is estimated and the propagation path is predicted by means of fracture mechanical simulation tools combined with the finite element analysis (FEA). We carry out a comprehensive parametric investigation of the cracking behavior of tungsten under typical transient thermal shock loads of ELM conditions but considering a wide range of load parameters. The main approaches are the J-integral method based on the virtual crack extension (VCE) technique and the extended finite element method (XFEM). The predicted crack patterns and the extent of crack growth are presented and discussed. Furthermore, the results of the two simulation methods, which are independent of each other, are compared. The quality of the predictions is discussed by comparing them with experimental data.

2. A brief review of the electron beam thermal shock tests for ELM simulation

The thermal shock loading conditions considered in the current simulation study were taken from the load parameters of the ELM simulation experiment conducted by Linke et al. [6]. In this chapter a brief summary of this experiment is given to foster understanding of the background of our computational study, since their experimental test was used as reference case for our FEA modelling. Detailed information to this test can be found elsewhere [6]. Linke's test campaign was carried out at the electron beam high heat flux test facility JUDITH at Forschungszentrum Jülich. Several different sorts of tungsten grades were tested including a tungsten grade following the ITER-specifications, ultra-high purity tungsten and W-Ta alloys. ELM loading situation were simulated with thermal loads ranging from 0.15 to 1.3 GW/m^2 with the duration of about one millisecond. The base temperature of the specimen was varied from 20 up to 800 °C. The key findings are:

1. Formation and growth of the surface cracks became more dominant as the base temperature was decreased.
2. There was a threshold base temperature above which no cracking took place but only plastic roughening of surface.
3. The cracks were initiated and extended in perpendicular direction to the surface.
4. Sometimes cracks changed their orientation during propagation deflecting from their initial path. The typical depth at which cracks kinked was between 200 and 600 μm.
5. Some cracks further grew far into depth whereas the others did not.
6. The density and length of the cracks was dependent on the applied load and base temperature.

It is noted that the cracking feature observed in this ELM-like high heat flux test study has generic qualitative validity to other electron beam-based thermal shock tests on tungsten. On the other hand, similar thermal shock tests

using plasma beam accelerator showed somewhat different cracking threshold loads [7]. A computational fracture mechanics study for the latter case has been performed by the present authors as well and will be published in the near future.

3. FE model

3.1. Geometry

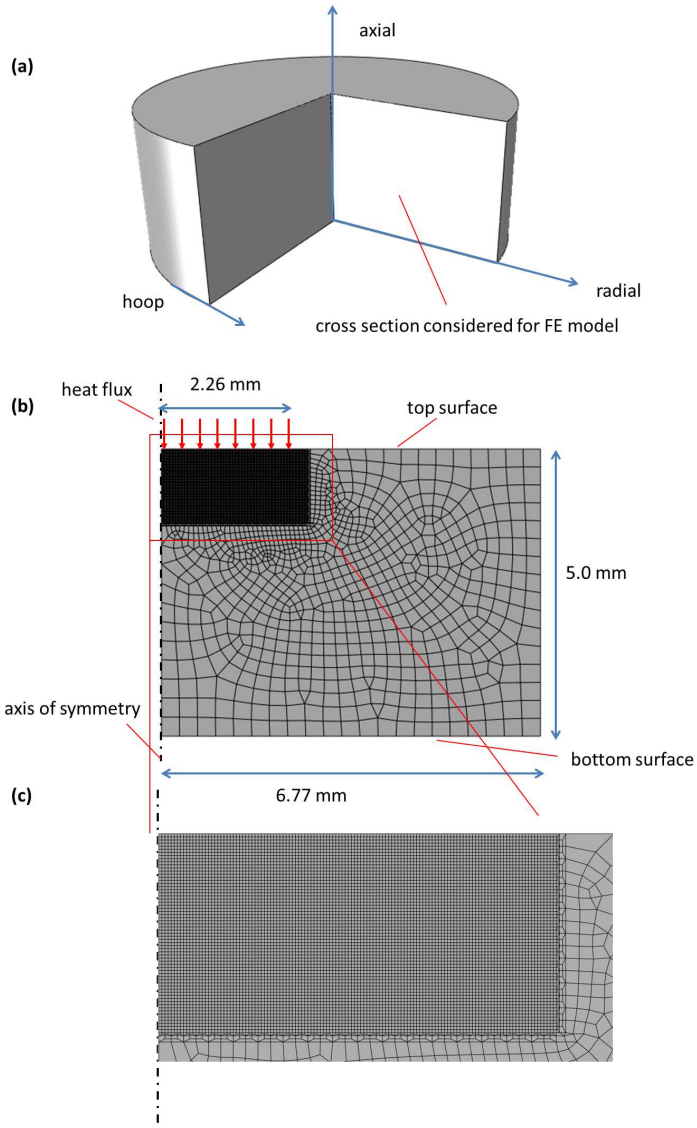

Fig. 1. (a) A schematic drawing of the model geometry, (b) two-dimensional FE model created for the right half of the vertical cross section. The mesh consists of axisymmetric elements reflecting the rotational symmetry of the model, (c) finer mesh in the vicinity of the region of heat flux loading.

The finite element (FE) model was built according to typical settings realized in thermal shock experiments at Forschungszentrum Jülich. Tungsten samples with dimensions of 12 mm × 12 mm × 5 mm were mounted on a heated

sample holder, so that the base temperature of the samples could be adjusted between room temperature and 800 °C. A nearly homogeneous heat flux load was achieved in a square of $4 \times 4\,\mathrm{mm}^2$ at the top surface of the sample by fast scanning of the surface with an electron beam. In the FE model, a disk shaped sample was considered instead of the real dimensions of the tungsten sample (see Fig. 1 a). The area of the top surface and the height of the disk model were the same as those of the tungsten sample. The loading area was assumed to be a circle with an area of $16\,\mathrm{mm}^2$ instead of a square loading area. A uniform heat flux load was assumed over the heat-loaded area for simplicity. As a consequence of these simplifications, a two-dimensional axisymmetric model could be set up for the right half of the vertical cross section considering the rotational symmetry of the model geometry, see Fig. 1 b. The advantage of the simplified model is that one can save computational efforts by reducing the dimension of the FE model, and one can avoid convergence problems possibly encountered in three-dimensional fracture mechanics simulations. The simulation tool for the computation was the commercial FEM code ABAQUS [8]. The finite element used in the simulations was a four-node axisymmetric quadrilateral element. To avoid mesh sensitive results, it is necessary to build a sufficiently fine mesh in the vicinity of the region of heat flux loading. There, the element edge size was 20 µm (see Fig. 1 c).

3.2. Materials

The numerical simulations in this work were performed in a continuum mechanics framework, and the material was assumed to be homogenous and isotropic. Thermal material parameters of tungsten, such as thermal conductivity, coefficient of thermal expansion and specific heat, and mechanical properties, such as Young's modulus and yield strength, refer to the data presented in literature [9, 10], and are listed in Tables 1 and 2.

Table 1. Thermal material parameters of tungsten at selected temperatures [9]

Temperature (°C)	Thermal conductivity (W/mK)	Density ($\mathrm{kg/m^3}$)	Specific heat (J/kgK)	Coefficient of thermal expansion (10^{-6}/K)
27	176	19299	133	4.74
927	114	19051	155	5.06
1927	99	18725	180	6.77
2727	92	18379	218	9.19

Table 2. Mechanical material parameters of tungsten at selected temperatures [10]

Temperature (°C)	Young's modulus (GPa)	Yield strength (MPa)
20	399	infinite[a]
200	391	1221
600	375	724
1000	356	467
1600	321	64
2000	278	42

[a] No value is reported in [10]. Here, it is assumed that tungsten behaves purely elastic at this temperature.

The values of yield strength and the ultimate tensile strength of tungsten are nearly the same [10]. Therefore, tungsten is assumed to behave elastic-ideally plastic in the simulations conducted in this work.

3.3. Loads and boundary conditions

The heat flux load was applied at the top surface of the tungsten sample to simulate the electron beam loading. When the electron beam is focused on a small spot at the sample surface, a very high power density is generated.

The kinetic energy of incident electrons is dissipated not only at the top surface but also deeper in the material. The electron beam penetration depth is dependent mainly on the energy of the electrons and the target material. For the loadings with 120 keV electrons and material relevant for this study, the penetration depth is less than 5 μm [3]. Therefore, the penetration of the electron beam was not considered in this work. The heat flux load was applied to the heating area at the top surface of the sample for 1 ms. According to the thermal calculation, the heat transfer between the bottom surface of tungsten and the sample holder has nearly no impact on the temperature at the top surface. For simplicity, a convective boundary condition was applied at the bottom surface. The power density of the electron beam loading is much larger than the energy loss due to radiation. As a result, the radiation effect can be neglected when calculating the temperature. To prevent rigid body movement, one node was fixed at the right corner of the model. In the simulation, the thermal excursion of tungsten consists of two steps, namely, 1 ms of heat flux loading and 10 s of cooling.

Cracking of tungsten was observed in single thermal shock experiments as well as multiple thermal shocks experiments [3, 4]. In experiments comprising up to 100 thermal shocks, the minimum crack distance was found to be larger than the maximum grain diameter. This indicates a brittle crack formation, since in thermal fatigue induced crack formation, the crack distances were not related to the grain diameter [5]. However, increasing the cycle number from 1 to 100 can cause the formation of numerous micro-cracks [11], which can lead to macro-cracks during further cycles.

In this work, the numerical simulations aim at simulating cracking induced by the brittleness of tungsten, whereas thermal fatigue damage was not considered. Furthermore, only one thermal cycle was simulated, for the reason mentioned above.

4. Results of the thermo-mechanical simulations

In this work, the heat transfer problem was solved first, then its solution was read into the corresponding mechanical simulation as a predefined temperature field.

4.1. Thermal simulations

Fig. 2 shows the surface temperatures a function of time for a power density of 1.27 GW/m^2 and a base temperature of 20 °C. The top surface is heated up to over 2500 °C within 1 ms, and after heating stops, the surface temperature is reduced to 1000 °C within 1 ms. This numerically gained observation is in accordance with analytical solutions reported in [12] for the one-dimensional heat conduction problem encountered when cooling down a sample whose infinite surface is heated by a heat source of finite size prior to cooling and was confirmed by surface temperature measurements by fast infrared and visible imaging in ELM simulation experiments [13]. Fig. 3 shows the sample temperature at different depths at the end of heating. Only the surface layer experiences a temperature above DBTT. At a depth of 480 μm, the maximum temperature is below 400 °C.

4.2. Mechanical simulations

Plastic strains are generated by the marked temperature variations in the loading area. During heating, the material in the loading area tends to expand due to the temperature increase, but it is constrained by the cold and rigid bulk material outside the loading area. Thus, the material in the loading area is in a compressive stress state, and compressive plastic strains are generated. During cooling, the material in the loading area shrinks rapidly due to the fast decrease of temperature. Shrinkage is constrained by the bulk material surrounding the loading area. As a result, the material in the loading area is subjected to tensile stresses.

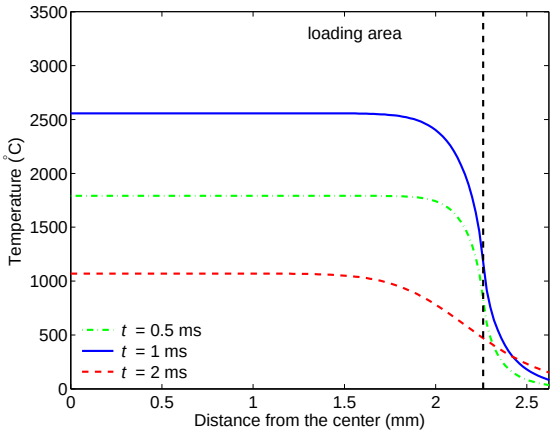

Fig. 2. Surface temperature at various moments, t, for a power density of 1.27 GW/m^2 and a base temperature of 20 °C.

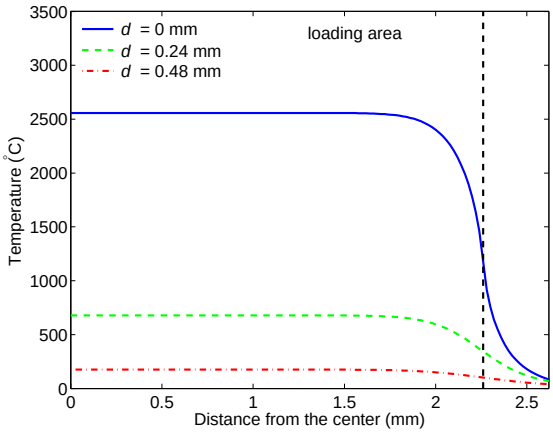

Fig. 3. Temperature at different depths, d, at the end of heating for a power density of 1.27 GW/m^2 and a base temperature of 20 °C.

Fig. 4 shows surface plastic strain in radial direction for a power density of 1.27 GW/m^2 and a base temperature of 20 °C at various moments. In the central part of the loading area, plastic strains generated by compressive stresses during heating are significantly reduced when the tungsten sample is cooled down. At the beginning of cooling, thermal stresses surpass the yield strength of tungsten, and plastic strains are generated by tensile stresses. Since the yield strength increases with decreasing temperature, tungsten behaves purely elastic upon further cooling. Plastic strains resulting from the tensile stresses cannot completely compensate plastic strains generated during heating, which indicates that tensile residual stress will be present. During cooling, much smaller plastic deformation is generated by tensile stresses near the edge of the loading area than in the center. As a result, the magnitude of the plastic strain near the edge of the loading area is larger than in the central part of the loading area at the end of cooling. At the edge of the loading area, a trough can be observed in the plastic strain distribution. Material that is subjected to less intensive temperature variations (e.g. deeper beneath the heat flux loading) will experience less or no plastic strain generated by tensile stresses during cooling. No trough exists in the plastic strain distribution (see the plastic strain at depths of 0.24 mm and 0.48 mm in Fig. 5).

Fig. 6 shows surface stress in radial direction as a function of the distance from the loading center. In the loading

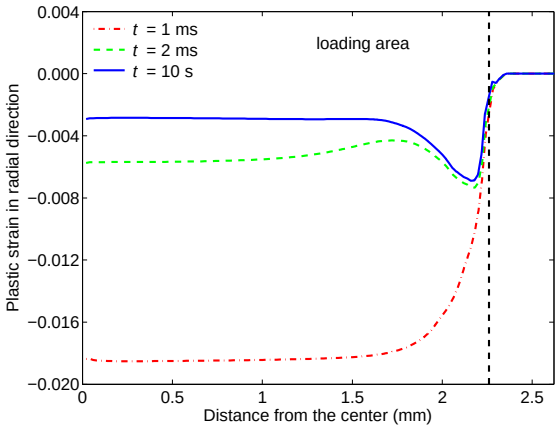

Fig. 4. Surface plastic strain in radial direction at various moments, t, for a power density of 1.27 GW/m^2 and a base temperature of 20 °C.

area, the surface stress in radial direction is compressive during heating ($t \leq 1$ ms) and tensile during cooling ($t > 1$ ms). Since tungsten is assumed to behave ideally plastic, the stress near the top surface during heating is limited by the small yield strength of tungsten at high temperature (see Table 2). After the sample is cooled down, high tensile residual stress is generated near the top surface. The peak stress in radial direction is observed near the edge of the loading area at the top surface. The out of surface deformation in the loading area is found at end of cooling, as shown in Fig. 7. The vertical displacement is qualitatively in good agreement with the results of a profilometry scan converted into a depth profile along the middle of the loading area in the thermal shock experiments [11]. Due to incompressibility of the material during plastic deformation, the region outside the loading area sinks down. The out of surface deformation and the sinking of material result in the tensile stress near the edge of the loading area. Furthermore, the compressive plastic deformation near the edge of the loading area is larger than in the central part of it. As a result, the stress in radial direction is larger near the edge of the loading area.

In Fig. 8, stress in radial direction along the axis of symmetry is shown for a power density of 1.27 GW/m^2 and a base temperature of 20 °C as a function of depth at the end of cooling. The stress increases slightly as depth increases till 0.2 mm, and then decreases with increasing depth. The stress profile along the perpendicular direction leads to bending of the sample. As a result, a compressive stress state can be observed when it is deeper than 0.4 mm.

Fig. 9 shows curves of stress-mechanical strain in radial direction at three positions, which are located at different depths along the axis of symmetry. The three curves at different depths represent three types of loading and unloading: purely elastic loading and unloading, plastic loading and elastic unloading, and plastic loading and unloading. Purely elastic loading and unloading occur if no plastic deformation is generated in the whole loading history, as represented by the stress-mechanical strain curve for a depth of 0.48 mm. Plastic loading and elastic unloading are defined when there is plastic behavior during heating but no plastic deformation is generated during cooling, see the stress-mechanical strain curve at a depth of 0.24 mm. If plastic deformation occurs both in the heating and the cooling parts, the resulting behavior is termed as plastic loading and unloading, see the stress-mechanical strain curve predicted for the top surface.

4.3. Effect of power density

To study the effect of power density, different power densities ranging from 0.3 GW/m^2 to 1.27 GW/m^2 were applied in the simulations. The base temperature is set to be 20 °C. Fig. 10 shows surface temperature at the end

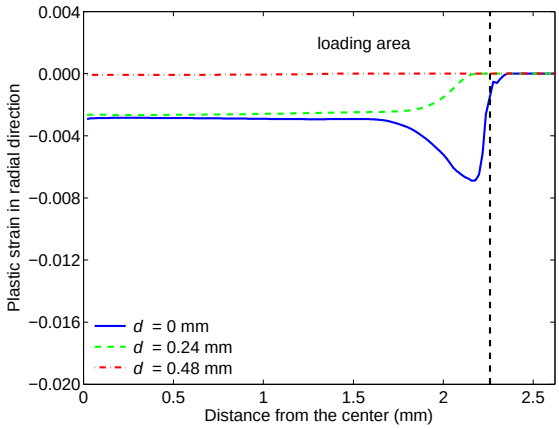

Fig. 5. Plastic strain in radial direction at different depths, d, at the end of cooling for a power density of 1.27 GW/m^2 and a base temperature of 20 °C.

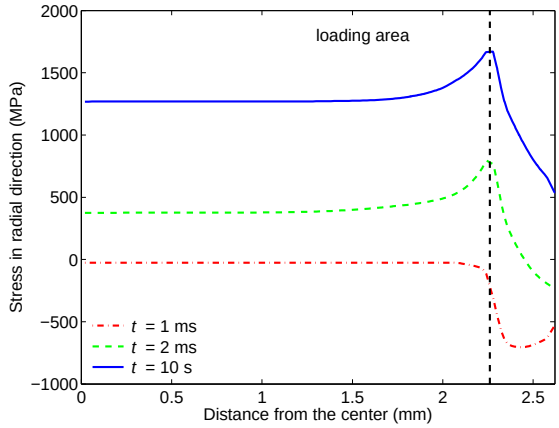

Fig. 6. Surface stress in radial direction at various moments, t, for a power density of 1.27 GW/m^2 and a base temperature of 20 °C.

of heating for several power densities. The maximum temperature is proportional to the power density. When the power density is larger than 0.6 GW/m^2, the maximum temperature is above DBTT of tungsten. Fig. 11 shows plastic strain in radial direction for different power densities. When the power density is large enough for plastic unloading, additional plastic strains resulting from an increase of power density are nearly the same in the heating and the cooling periods. As long as plastic unloading occurs at the top surface, plastic strains in the central part of the loading area will therefore be identical. For power densities between 0.6 GW/m^2 and 1.27 GW/m^2, nearly identical plastic strains in radial direction are found in the central part of the loading area. When loading with 0.3 GW/m^2, plastic strain in radial direction is much smaller. Thus, the threshold power density for plastic unloading lies between 0.3 GW/m^2 and 0.6 GW/m^2. The trough in the plastic strain distribution curve becomes deeper as power density increases.

Fig. 12 shows surface stress in radial direction at the end of cooling for different power densities and a base temperature 20 °C. For a power density of 0.3 GW/m^2, the stress in radial direction is much smaller than for the loadings above the threshold power density for plastic unloading. For loadings between 0.6 GW/m^2 and 1.27 GW/m^2 the peak stress increases as the power density increases. However, tensile stress in the central part of the loading area

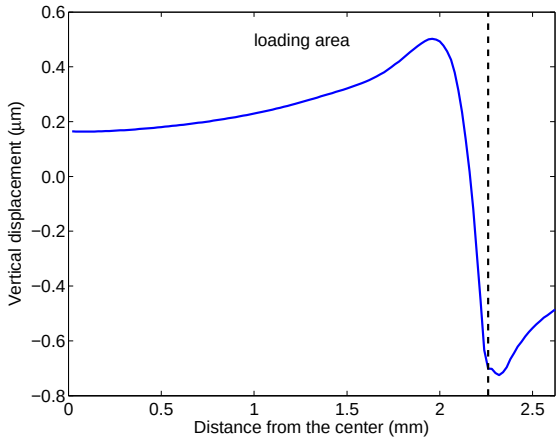

Fig. 7. Surface vertical displacement at the end of cooling for a power density of 1.27 GW/m^2 and a base temperature of 20 °C.

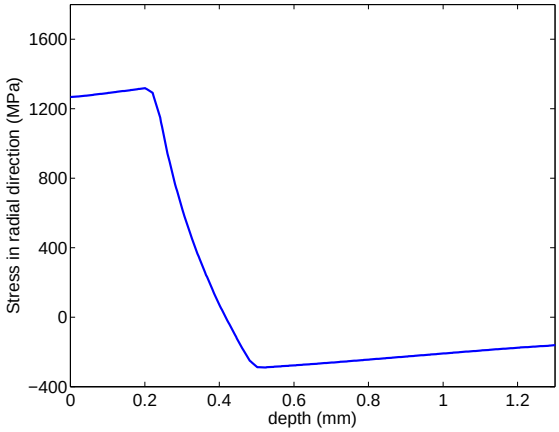

Fig. 8. Stress in radial direction as a function of depth, *d*, at the end of cooling for a power density of 1.27GW/m^2 and a base temperature of 20 °C.

decreases slightly as power density increases.

4.4. Effect of base temperature

Due to the strong temperature dependence of tungsten's physical properties, the base temperature of the sample plays an important role for the behavior of tungsten under heat flux loadings. In the course of this work, base temperatures ranging from 20 °C to 800 °C were applied. The base temperatures are used to mimic the temperature induced by the stationary thermal loading. Thus, the simulations under short transient thermal loads with a high base temperature serve to estimate the conditions of tungsten being exposed to both stationary and transient thermal loads. Fig. 13 illustrates surface temperature at the end of heating for different base temperatures. The surface temperature increases as base temperature increases. When the base temperature reaches 800 °C, the maximum temperature is close to the melting point of tungsten (3422 °C) for a power density of 1.27 GW/m^2.

In Fig. 14, surface plastic strain in radial direction is shown at the end of cooling for different base temperatures. In the central part of the loading area, the magnitude of plastic strain in radial direction decreases as the base temperature

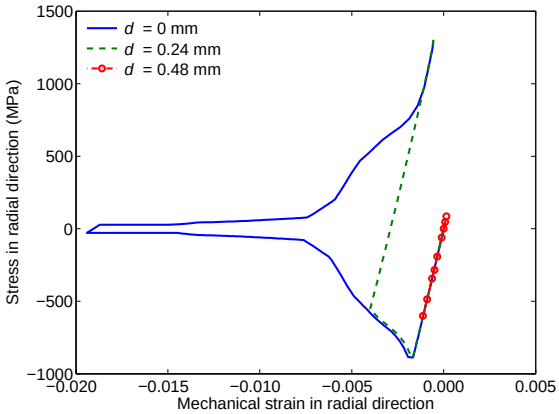

Fig. 9. Stress-mechanical strain in radial direction at different depths, d, for a power density of 1.27 GW/m^2 and a base temperature of 20 °C.

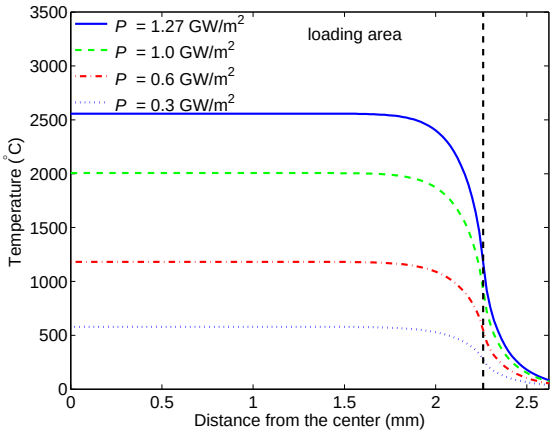

Fig. 10. Surface temperature at the end of heating for different power densities, P, and a base temperature of 20 °C.

increases. The reason for this is that by increasing base temperature, the increase of plastic formation during heating is smaller than during cooling. The plastic strain in radial direction occurs outside the loading area, when the base temperature is above 400 °C. The trough in the plastic strain distribution curve is deeper for a higher base temperature. Fig. 15 shows equivalent plastic strain for different base temperatures. The equivalent plastic strain increases as base temperature increases, which indicates that thermal fatigue damage is more likely to occur for a higher base temperature under repeated heat flux loads. Surface stress in radial direction at the end of cooling is plotted in Fig. 16.

5. Fracture mechanics simulations

5.1. XFEM simulations

Using the conventional finite element method, modeling stationary discontinuities requires boundary-conforming meshes for geometrically discontinuous domains, and the corresponding mesh refinement involves considerable computational efforts. However, XFEM alleviates the shortcomings associated with meshing crack surfaces.

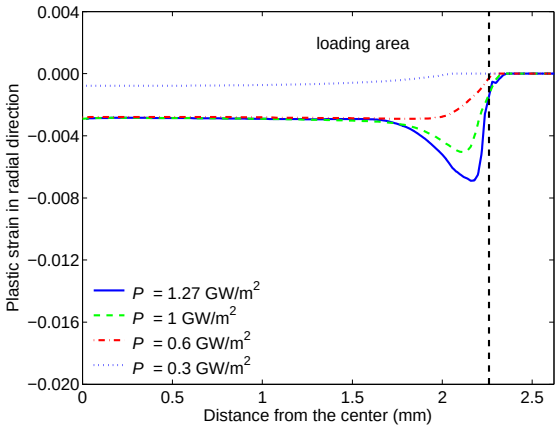

Fig. 11. Surface plastic strain in radial direction at the end of cooling for different power densities, P, and a base temperature of 20 °C.

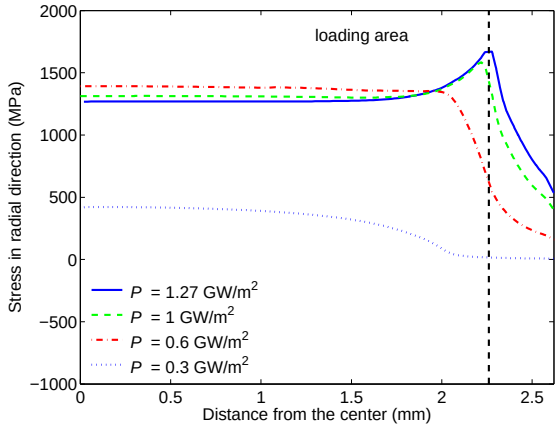

Fig. 12. Surface stress in radial direction at the end of cooling for different power densities, P, and a base temperature of 20 °C.

XFEM was first introduced by Belytschko and Black [14]. It is an extension of the conventional finite element method based on the concept of so-called enrichment functions which enable modeling discontinuities such as cracks without any discrete mesh adaption.

To simulate crack initiation and propagation using XFEM, a maximum principal stress (MPS) criterion and an energy based damage evolution law are needed. Once the principal stress exceeds the maximum allowable value, a crack is initiated. At the same time, there is a degradation of the cohesive stiffness in the elements in which the crack formation occurs, which can be described by the energy based damage evolution law. If the energy dissipation associated with crack extension is larger than the fracture energy, the cohesive stiffness becomes zero, and the crack opens up completely. The value of the ultimate tensile strength can in principle be used as an estimate for the MPS. The ultimate tensile strength of tungsten in the vicinity of DBTT (400 °C-700 °C) is about 900 MPa-700 MPa [10]. Considering that crack formation is mainly due to the brittleness of tungsten below DBTT, the MPS is defined to be 900 MPa. For the fracture energy in the course of damage evolution, 0.25 mJ/mm^2 is used, which is transferred from the fracture toughness obtained from the test performed at 400 °C by Gludovatz et al. [15] applying the concept of

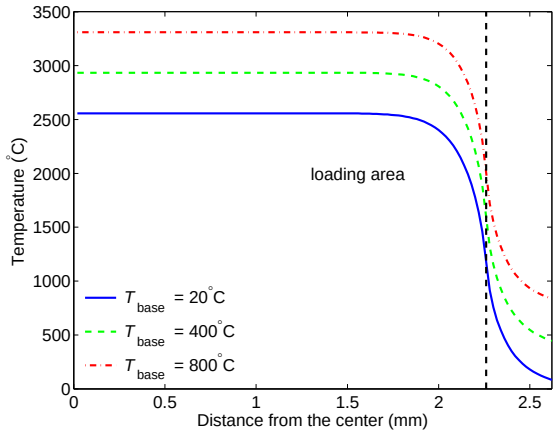

Fig. 13. Surface temperature at the end of heating for different base temperatures, T_{base}, and a power density of 1.27 GW/m^2.

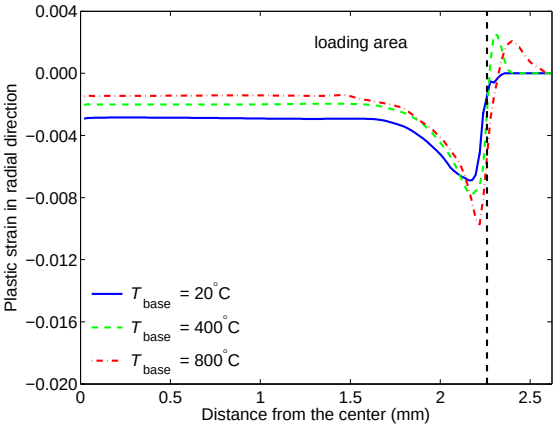

Fig. 14. Surface plastic strain in radial direction at the end of cooling for different base temperatures, T_{base}, and a power density of 1.27 GW/m^2.

linear elastic fracture mechanics.

To avoid a possible influence by multiple cracks, the XFEM simulations were first carried out by introducing a single precrack of 20 µm length, and no other crack initiation was allowed. Fig. 17 shows the crack propagation predicted by introducing precracks at different positions for a power density of 1.27 GW/m^2. Precracks positioned in the central part of the loading area propagate perpendicularly to the loading surface, while a precrack near the edge of the loading area grows parallel to the loading surface at a depth of about 500 µm, which coincides well with experimental findings [4]. A precrack near the edge of the loading area grows towards the center of the loading area because it experiences both tensile and shear loads, while in the central part of loading the stress field is near purely tensile. When multiple thermal shocks are applied, the crack opening resulting from the previous thermal shock will change the stress and strain distributions, so that the stress field may not be purely tensile in the central part of the loading area. As a result, crack growth parallel to the loading surface may also occur in the central part of the loading area.

Fig. 18 shows the cracks predicted using XFEM for loadings of different power densities allowing occurrence of

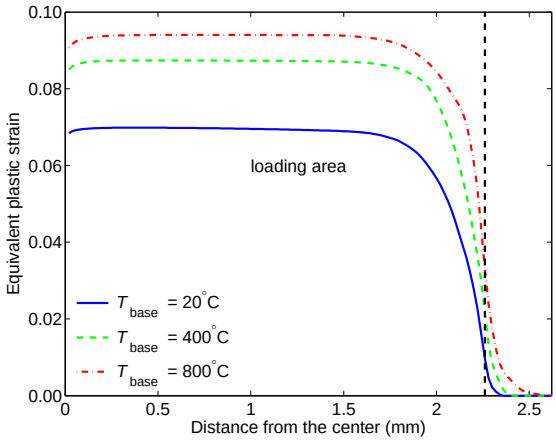

Fig. 15. Equivalent plastic strain at the end of cooling at the top surface for different base temperatures, T_{base}, and a power density of 1.27 GW/m^2.

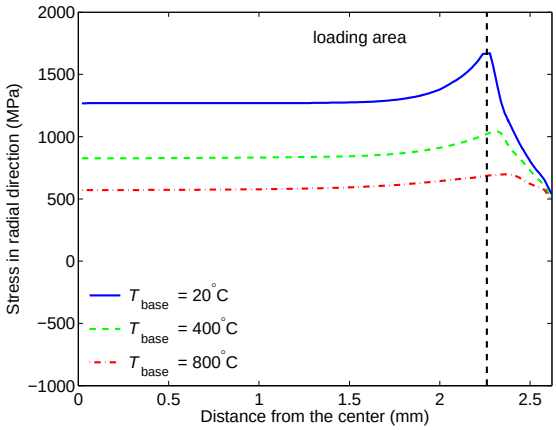

Fig. 16. Surface stress in radial direction at the end of cooling for different base temperatures, T_{base}, and a power density of 1.27 GW/m^2.

multiple cracks. It is seen that some cracks in the central part of the loading area are not initiated at the surface but at some depth below the surface (roughly at 0.2 mm depth). This feature can be understood from the depth profile of the radial stress component. The maximum radial stress occurs exactly in the depth range where the cracks are mostly populated without surface cracking (see Fig. 8). Cracks in the central part of the loading area are perpendicular to the loading surface and not fully opened. However, in the XFEM simulations with a single crack, the crack in central part of the loading area is much longer and fully opened (see Fig. 17), since when multiple cracks are initiated in the central part of the loading area, the stiffness is degraded in such a way that the stress concentration at the crack tips is not as intensive as in the XFEM simulations with a single crack. For the loadings with 1.27 GW/m^2 and 1 GW/m^2, cracks are generated near the edge of the loading area and propagate parallel to the loading surface. For a power density of 0.6 GW/m^2, no crack is formed near the edge of the loading area, as there is no stress concentration, see Fig. 12. No crack initiation is found for the loading with 0.3 GW/m^2, since the stress is much smaller than the MPS. The XFEM results are capable of reproducing the main cracking features observed in the experiments [4].

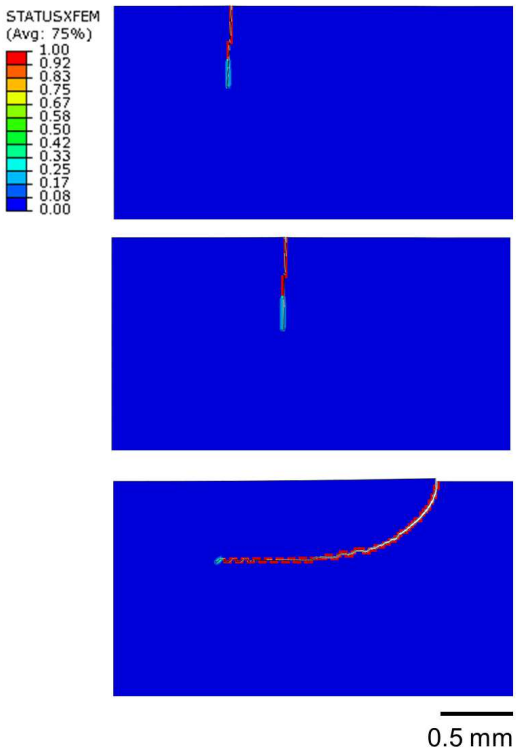

Fig. 17. Cracks predicted using XFEM by introducing a single precrack at different locations (top: 0.8 mm away from the center, middle: 1.2 mm away from the center, bottom: 2.24 mm away from the center) for a power density of 1.27 GW/m^2 and a base temperature of 20 °C. The quantity STATUSXFEM characterizes damage evolution. A value of 1.0 characterizes an opened crack. Positive values smaller than 1.0 stand for cracks that require additional energy to be opened.

5.2. J-integral calculation

In the framework of fracture mechanics, the onset of crack growth is thought to be dictated by singular stress intensity at the crack tip. Here, cracking process is controlled by an energy balance between the energy absorption rate needed to create new crack faces (surface energy) and the energy release rate caused by stress relaxation (stored strain energy). In this circumstance, the quantity of released strain energy is described by a path-independent local contour integral around the crack tip called *J*-integral. The *J*-integral was first developed by Rice [16] and is a measure of driving force for crack extension in a similar sense that stress intensity factor stands for crack tip loads. In this context, a conjugate material parameter 'critical *J*-integral (J_c)' (or fracture energy) is defined, which represents a measure of material's resistance against crack extension. For a given local stress fields and crack configuration, a crack begins to grow as soon as the *J*-integral exceeds its critical value. The *J*-integral is numerically attractive, since it can be evaluated by a path independent contour integral. To evaluate these contour integrals for computing *J*-integrals, the domain integral method is used, which is quite robust in the sense that accurate contour integral estimates are usually obtained even with quite coarse meshes. In this work, the *J*-integral is calculated with the FEM-based VCE method at the end of cooling, when the material behaves purely elastic. If plasticity occurs, the *J*-integral calculation is also possible by describing the elasto-plastic material as an "equivalent elastic material" [8]. However, the residual stress influence must be considered, otherwise the *J*-integral will not be path-independent. In ABAQUS [8], the residual stress field is treated as an initial strain field so that a path-independent *J*-integral can be obtained .

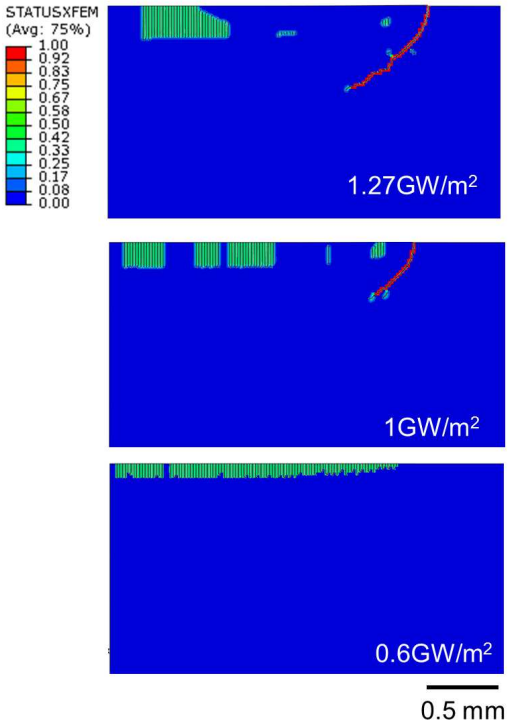

Fig. 18. Cracks predicted using XFEM with occurence of multiple cracks for different power densities and a base temperature of 20 °C.

In both the thermal shock experiments and the XFEM simulations, most cracks are perpendicular to the loading surface. To calculate J-integrals for these cracks, precracks are defined to be perpendicular to the loading surface. J-integrals are calculated at the end of cooling, and plastic strains at end of cooling are considered to be initial strains. The direction of the virtual crack tip extension points into the sample. Length and location of precracks (see Fig. 19) are variables for a parametric study. To avoid the influence from other cracks, only one precrack is allowed in each calculation.

Fig. 20 shows J-integral for precracks at different positions. At first J-integrals increase with the crack length up to a crack length of 0.1 mm, because stress does not decrease with increasing depth within the depth of 0.1 mm. Then, J-integrals decrease with increasing crack length due to the decrease of stress. The J-integral is smaller when the precrack is close to the axis of symmetry, since the driving force for crack opening is reduced at the crack surface close to the center due to axisymmetric modelling. Table 3 lists the crack opening displacement (COD) of precracks of 0.08 mm length. The COD shows the same tendency as the J-integral. In the thermo-mechanical simulations it is shown that a peak stress occurs near the edge of the loading area. However, there is no peak value of the J-integral near the edge of the loading area to be seen in Fig. 20, since the stress concentration is relaxed when a precrack is inserted near the edge of the loading area, and nearly no stress is generated at the crack surface close to the bulk material outside the loading area, as the material is separated from the loading area by the precrack.

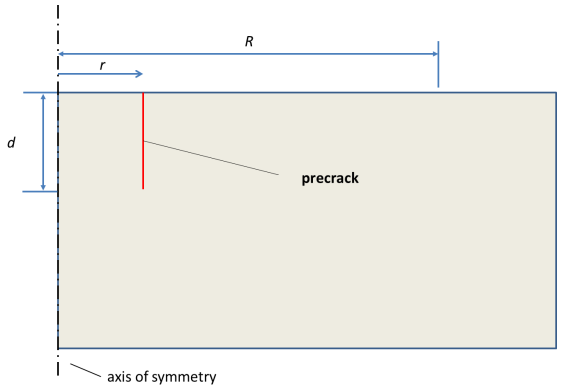

Fig. 19. Precrack for the calculation of the J-integral.

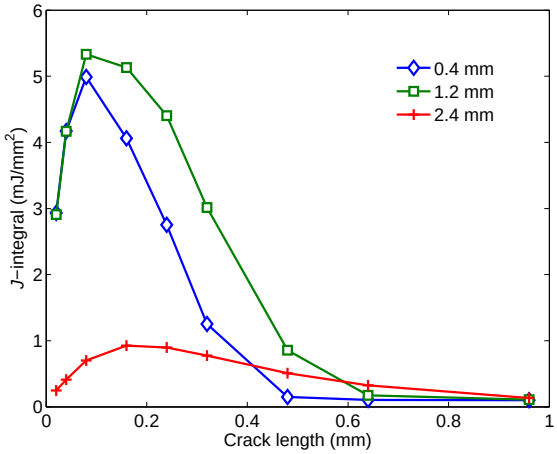

Fig. 20. J-integral for a power density of 1.27 GW/m^2 and a base temperature of 20 °C. Different distances (0.4 mm, 1.2 mm and 2.4 mm) of the precrack from the center of the loading area are considered.

5.3. Effects of base temperature and power density on the J-integral

In this work, a parametric study of base temperatures (20 °C to 800 °C) and power densities (0.3 GW/m^2 to 1.27 GW/m^2) serves to study their effects on the value of the J-integral. In order to predict cracking at different base temperatures, a temperature dependent critical value of the J-integral (J_c) is needed. Gludovatz et al. [15] measured the fracture toughness (K_{Ic}) of tungsten. However, at room temperature, the fracture toughness of rolled tungsten determined by Gludovatz et al. varies from 4.69 MPa $\sqrt{m}$ to 9.08 MPa $\sqrt{m}$ by changing the compact tension specimens to 3-point bending specimens [15]. As-sintered tungsten exhibits a fracture toughness of 5.1 MPa $\sqrt{m}$ using compact tension specimens. The fracture toughness of the polycrystalline tungsten rods at room temperature is 8.0±0.2 MPa $\sqrt{m}$ for transverse and 12.6±1.3 MPa $\sqrt{m}$ for longitudinal specimens[1] [17]. Hence, the fracture toughness of tungsten varies by at least a factor of two depending on both manufacturing method of the tungsten samples and the testing procedure. Taking this span of values into account when deriving the critical value of J_c from the tem-

[1]For transverse specimens, the long axis is parallel to the swaging direction, while the long axis of longitudinal specimens is perpendicular to the swaging direction.

Table 3. Crack opening displacement of precracks of 0.08 mm length

Distance from the center (mm)	0.4	0.8	1.2	1.6	2.0	2.4
Crack opening displacement (μm)	7.5	7.78	7.69	7.41	5.42	1.03

perature dependent fracture toughness data determined by Gludovatz et al. [15] allows to study the impact of reported fracture toughness values and temperature on the cracking behavior.

Fig. 21 shows values of the J-integral for different power densities and base temperatures. In these studies a precrack positioned 1.2 mm away from the loading center is chosen to represent a general situation in the central part of the loading area, because the precrack is situated far enough from both the axis of symmetry and the edge of the loading area. In general, the J-integral increases as power density increases. Higher base temperatures lead to smaller stresses. As a consequence, J-integrals are smaller too. At low base temperatures (e.g. below 200 °C) and for power densities larger than 0.6 GW/m^2, the J-integrals are much larger than both values of J_c, which indicates that cracking can be hardly avoided at low base temperatures. However, since the fracture toughness of tungsten increases with increasing the temperature, the J-integrals calculated for a base temperature of 800 °C are much smaller than the critical value. Thus, high base temperatures are suitable to prevent crack opening. Nevertheless, one must keep in mind that increasing the base temperature will also lead to an increase in the equivalent plastic strain that describes the plastic deformation history. This in turn may cause material degradation and thermal fatigue failure. Other than that, a high base temperature might lead to a surface temperature that is close to or even higher than the melting point of tungsten so significantly degrading the structural integrity of the component.

Fig. 22 shows the thermal shock behavior based on J_c gained from both the fracture toughness obtained by Gludovatz et al. [15] and its doubled value. In our analysis a crack is defined as such if the J-integral for a precrack of 20 μm length is larger than J_c. This specific crack length of 20 μm is assumed to be the crack length that can be developed from the initial defects along the grain boundaries without reaching the critical value of the energy release rate, since grain boundaries are more vulnerable than the grain interior. This assumption yields a slightly conservative estimation in cases that there are very few initial defects at the top surface of the tungsten sample near a stress concentration or the initial defects cannot grow to become a crack of 20 μm length. In Fig. 22, there are no essential changes concerning the cracking threshold even if the value of the fracture toughness assumed for computing J_c is doubled. This indicates that in order to avoid cracking of tungsten at low temperatures, the fracture toughness of tungsten needs to be improved significantly. The threshold power density is between 0.3 GW/m^2 and 0.6 GW/m^2, and the threshold base temperature is between 400 °C and 600 °C. The numerically predicted thresholds coincide roughly with the experimental observations [6], where the experimentally determined threshold power density is between 0.16 GW/m^2 and 0.4 GW/m^2 and the threshold base temperature is between 100 °C and 400 °C depending on the tungsten grade tested.

Deviations between the cracking thresholds obtained from the experiments and the J-integral calculations are to be expected, since the material data used in this work may differ from the tungsten properties after thermal loadings - and also because the difference of material properties resulting from different fabrication processes is not included in the calculations. Furthermore, it should be noted that the thermal shock behavior obtained from the experiments considers 100 thermal shocks. The evolutions of microstructure and material parameters with the thermal cycles, which are not taken into consideration in the J-integral calculation, may also influence the results.

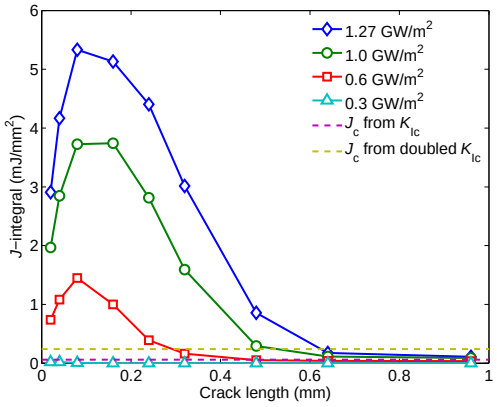

(a) base temperature 20 °C

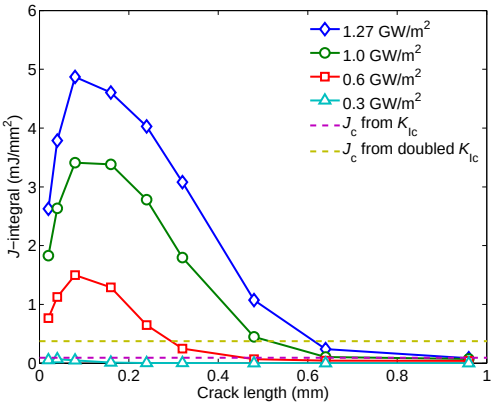

(b) base temperature 200 °C

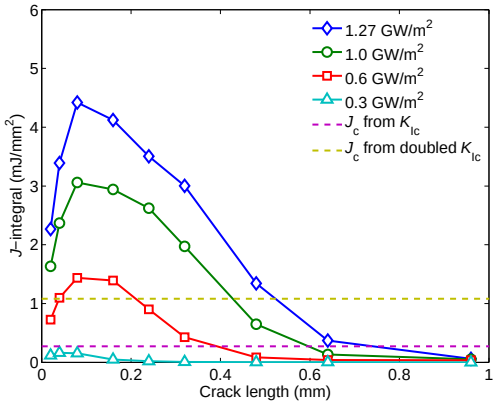

(c) base temperature 400 °C

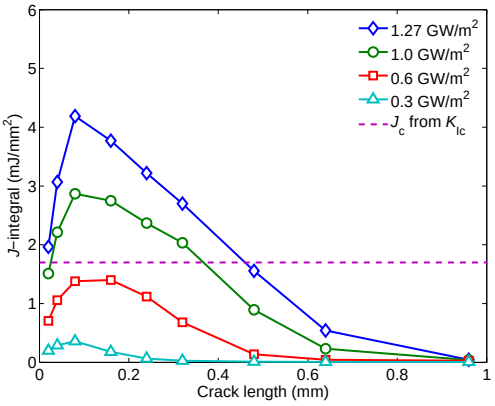

(d) base temperature 600 °C

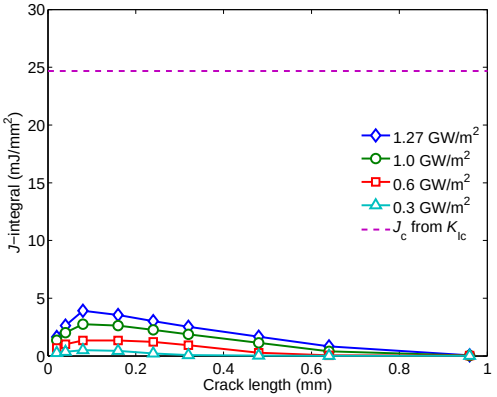

(e) base temperature 800 °C

Fig. 21. J-integral for power densities of 0.3-1.27 GW/m^2 and base temperatures of 20 °C-800 °C. The precrack is set 1.2 mm away from the center. The value of J_c determined from the doubled fracture toughness are larger than the upper scale of the plots for base temperatures of 600 °C and 800 °C, and are, therefore, not shown in plots (d) and (e).

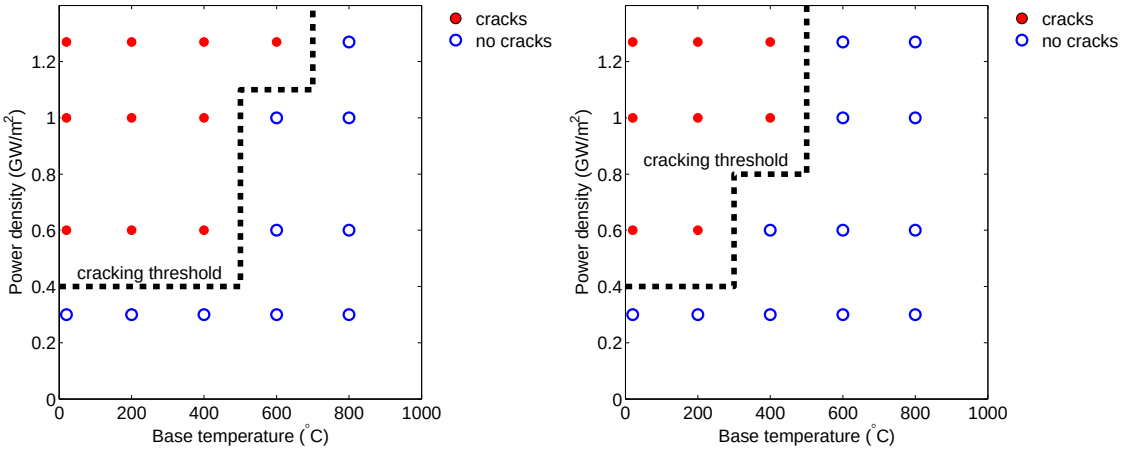

Fig. 22. Thermal shock behavior of tungsten samples calculated by comparing J-integrals with J_c gained from both the fracture toughness obtained by Gludovatz et al. [15] (left) and its doubled value (right).

6. Summary and conclusions

In this paper the cracking behavior of tungsten under transient thermal shock loads was investigated on the basis of rigorous computational fracture mechanical analysis combined with the finite element method. As loading conditions ELM-like loads were applied considering a relevant range of power density and base temperature for the parametric assessment. To this end, two independent theoretical tools were employed, namely, the virtual crack extension method for J-integral calculation and the extended finite element method for predicting crack initiation and progressive growth. To elucidate the results of the fracture mechanics analysis, a comprehensive analysis of stress and strain fields was undertaken. The present study delivered the following conclusions:

1. Upon cooling, tensile stress develops in the loaded surface layer as a consequence of plastic yield, coined as residual stress at the end of the cooling process. The radial component of tensile stress shows its maximum peak at the boundary of the loading area. At this position, a crack most probably first propagates in vertical direction, followed by a gradual horizontal kinking, parallel to the loading surface. Such cracking characteristics are typical for a power density of $1\,\mathrm{GW/m^2}$ and higher.
2. There is a threshold value of the heat flux load above which significant plastic flow takes place during both heating and cooling - and above which almost identical plastic strain and tensile stress are generated at the end of cooling. This threshold ranges between $0.3\,\mathrm{GW/m^2}$ and $0.6\,\mathrm{GW/m^2}$ at a base temperature of $20\,^{\circ}\mathrm{C}$.
3. The maximum peak value of the tensile residual stress (radial component) increases as the power density of the heat load is increased.
4. When the critical stress for crack initiation is reduced, many small cracks are formed in perpendicular direction to the surface over the whole loading area, especially in the central region. Once these cracks are initiated and continue to grow in the central part, the driving force for cracking near the boundary of the loading area is reduced.
5. The crack formation is predicted for the power density of $0.6\,\mathrm{GW/m^2}$ and above, and when the base temperature is higher than $600\,^{\circ}\mathrm{C}$, almost no crack is predicted.
6. The predicted threshold values of power density and base temperature for cracking agree roughly with the experimental observations. There are no essential changes concerning the cracking threshold even if the value of fracture toughness assumed for the simulation is increased by the factor of two.

In real fusion operation, high-heat-flux load comes from energetic bombardment of hydrogenic plasma particles. The chemical effect due to the presence of implanted hydrogen solute will have only limited impact on the crack behavior, provided that surface temperature during stationary operation remains above $800\,^{\circ}\mathrm{C}$ (as foreseen in ITER). In this case, hydrogen solute will not be able to be stably trapped by defects near the surface due to strong thermal vibration.

In this paper, isotropic properties were assumed for the sake of simplicity. The microstructure-related anisotropy in plastic and fracture properties will be a potential topic of future study.

References

[1] T. Hirai, K. Ezato, P. Majerus, Mater. Trans. 46 (2005) 412–424.
[2] A. Raffray, R. Nygren, D. Whyte, S. Abdel-Khalik, R. Doerner, F. Escourbiac, T. Evans, R. Goldston, D. Hoelzer, S. Konishi, P. Lorenzetto, M. Merola, R. Neu, P. Norajitra, R. Pitts, M. Rieth, M. Roedig, T. Rognlien, S. Suzuki, M. Tillack, C. Wong, Fusion Eng. Des. 85 (2010) 93–108.
[3] T. Hirai, G. Pintsuk, J. Linke, M. Batilliot, J. Nucl. Mater. 390-391 (2009) 751–754.
[4] G. Pintsuk, A. Prokhodtseva, I. Uytdenhouwen, J. Nucl. Mater. 417 (2011) 481–486.
[5] M. Wirtz, J. Linke, G. Pintsuk, L. Singheiser, I. Uytdenhouwen, Phys. Scr. T145 (2011) 014058.

[6] J. Linke, T. Loewenhoff, V. Massaut, G. Pintsuk, G. Ritz, M. Roedig, A. Schmidt, C. Thomser, I. Uytdenhouwen, V. Vasechko, M. Wirtz, Nucl. Fusion 51 (2011) 073017.
[7] I. Garkusha, I. Landman, J. Linke, V. Makhlaj, A. Medvedev, S. Malykhin, S. Peschanyi, G. Pintsuk, A. Pugachev, V. Tereshin, J. Nucl. Mater. 415 (2011) 481–486.
[8] Abaqus Analysis User's Manual 6.12., Dassault Systémes Simulia Corp., Providence, RI, USA (2012).
[9] Siemens AG, Internal report on physical parameters of tungsten (1995).
[10] PLANSEE, Tungsten Material Properties and Applications, http://www.plansee.com/en/Materials-Tungsten-403.htm (2014).
[11] I. Uytdenhouwen, Degradation of first wall materials under ITER relevant loading conditions, Ph.D. thesis, University Gent, 2011.
[12] H. S. Carslaw, J. C. Jaeger, Conduction of Heat in Solids, 2nd ed., Oxford University Press, New York, 1959.
[13] G. D. Temmerman, J. Zielinski, S. van Diepen, L. Marot, M. Price, Nucl. Fusion 51 (2011) 073008.
[14] T. Belytschko, T. Black, Int. J. Numer. Meth. Engng 45 (1999) 601–620.
[15] B. Gludovatz, S. Wurster, A. Hoffmann, R. Pippan, 17th Plansee Seminar (2009).
[16] J. R. Rice, J. Appl. Mech. 35 (1968) 379–386.
[17] P. Gumbsch, J. Nucl. Mater. 323 (2003) 304–312.